Numerical and Experimental Investigation of Flow Confinement Effects on UAV Rotor Noise

Clément Nardari[*], Damiano Casalino[†] and Francesco Polidoro[‡]
Dassault Systèmes Simulia Corp., 175 Wyman St., Waltham, MA, 02451

Vedran Coralic[§], John Brodie[¶] and Phoi-Tack Lew[‖]
Amazon.com Inc., 410 Terry Ave. N, Seattle, WA, 98109

The primary objective of the present study is to investigate the impact of the recirculating flow that develops inside a closed, hemi-anechoic test chamber on the noise generation mechanisms of a drone rotor operated under static thrust conditions. To that end, Lattice-Boltzmann simulations are conducted for both an idealized, semi-infinite free-field and a confined, hemi-anechoic domain that models the test chamber, with the latter validated against experimental measurements. Comparison between simulations reveals a significant increase in rotor noise due to confinement, up to 5 dBA in overall sound pressure level depending on microphone location, with negligible impact on aerodynamic performance. Blade-strip and beam-forming source identification techniques are utilized to determine those sound-generation mechanisms responsible for the increase in rotor noise. Leading-edge interactions between the vortical structures convected by the recirculating flow and the rotor's blades are demonstrated to be directly responsible for the generation of unsteady loads that lead to significantly higher blade passing frequency harmonic peaks. A small enhancement of the high-frequency self-noise contribution is also observed, whereas blade-tip vortex dynamics are largely unaffected by confinement so that the contribution of blade-vortex interaction noise is negligible.

I. Nomenclature

BPF   =   blade passing frequency
c =   blade section chord
C_Q =   torque coefficient, $C_Q = \frac{Q}{\rho n^2 D^5}$
C_T =   thrust coefficient, $C_T = \frac{T}{\rho n^2 D^4}$
D =   rotor diameter
f =   frequency
k =   turbulent kinetic energy
L_x =   hemi-anechoic chamber length
L_y =   hemi-anechoic chamber width
L_z =   hemi-anechoic chamber height
M_c =   chord-based Mach number
N =   1/3-Octave band number
n =   rotor angular speed
OASPL   =   overall sound pressure level, relative to reference level of 2×10^{-5} Pa
PWL   =   power Watt level, relative to reference level of 10^{-12} W
Q =   rotor torque
Re_c =   chord-based Reynolds number
SPL   =   sound pressure level, relative to reference level of 2×10^{-5} Pa

[*]Senior Aerospace Engineer, SIMULIA, clement.nardari@3ds.com
[†]Senior Technical Director, SIMULIA, damiano.casalino@3ds.com
[‡]Senior Technical Director, SIMULIA, francesco.polidoro@3ds.com
[§]Senior Research Scientist, Prime Air, vcoralic@amazon.com
[¶]Senior Mechanical Engineer, Prime Air, brodiej@amazon.com
[‖]Research Scientist, Prime Air, phoitack@amazon.com

T	=	rotor thrust
y^+	=	dimensionless wall distance
ε	=	turbulent dissipation rate
λ_2	=	lambda-2 vortex criterion
ρ	=	fluid density

II. Introduction

THE future of urban air mobility is evolving toward electric vertical take-off and landing (eVTOL) vehicles, which most prominently have promising applications in transportation and delivery. eVTOL vehicle concepts typically rely on rotors for propulsion, naturally raising concerns over the noise they might generate as they fly over populated areas. Then, for such vehicles to be both accepted by the public and still satisfy their concept of operations, it is imperative that their rotors be both low-noise and efficient, two objectives that are frequently at odds with one another.

An effort to optimize rotor aeroacoustics and aerodynamics typically begins with low-fidelity models of both. The low-fidelity models are utilized to reduce the design space to a manageable number of candidate rotors, which can then be evaluated with a high-fidelity model and, eventually, manufactured and tested in an anechoic facility. The validation of rotor performance predictions using anechoic facility measurements can be a challenge, however, since the typically closed environment of the facility differs significantly from the free-field conditions usually assumed by low- and high-fidelity models. Indeed, in a recent experimental investigation, Stephenson *et al.* [1] showed that the flow recirculation that occurs inside a closed anechoic chamber results in significantly higher rotor noise than is otherwise measured in the absence of recirculation. A potential pitfall in the rotor design process, then, is that the low- and high-fidelity models will produce candidate designs whose performance cannot be validated in the anechoic facility and/or that, when tested therein, do not outperform previous design iterations.

In their study, Stephenson *et al.* [1] argued that the test conditions inside a closed anechoic facility are not representative of the environment in which a rotor will operate, suggesting, as remedy, that mesh treatments be utilized to disrupt recirculation. While Stephenson *et al.*'s argument is sensible, it is also important to acknowledge that a rotor will generally not operate under ideal conditions either, but will routinely be subject to wind turbulence, ground effects, *etc.* in day-to-day operations. In this context, a closed anechoic facility, absent of mesh treatments, provides relevant test conditions for assessing rotor performance. It also makes for a more challenging environment to optimize rotor aerodynamics and aeroacoustics in, which may lead to more robust designs. The motivation for the present study, then, is to understand how the effects of the anechoic chamber on the rotor's performance can be accounted for in low- and high-fidelity models, so that these yield candidate designs that not only can be validated with in-chamber measurements, but can also be expected to perform well both at on- and off-design operating conditions.

To that end, and as a first step, we perform both experiments and simulations of a rotor operating under static thrust conditions inside a closed, hemi-anechoic test chamber and investigate the impact of the recirculating flow on the rotor's noise generation mechanisms. High-fidelity, Lattice-Boltzmann method (LBM) simulations are carried out for both an idealized, semi-infinite free-field and a confined, hemi-anechoic domain that models the test chamber. The simulation results from the confined domain are validated using experimental measurements and are compared to the simulation results from the unconfined domain in order to clearly identify and characterize the effects of flow recirculation.

III. Experimental Methodology and Procedures

A. Hemi-anechoic Chamber

Amazon Prime Air's hemi-anechoic chamber was utilized to measure the noise produced by the propeller. A schematic of the facility is sketched out in Fig. 1. The chamber is $L_x = 8.76D$ long, $L_y = 8.86D$ wide and $L_z = 7.79D$ tall, where D is the rotor diameter. Its walls and ceiling are treated with anechoic foam paneling, while the floor – a thick concrete slab – is left untreated and reflective. Our calibration experiments indicate that the chamber is hemi-anechoic within ±1 dB above a blade passing frequency (BPF) harmonic of 2.2, but only within ±4 dB below that, primarily due to the onset of standing waves, which are a consequence of the nearly cuboidal shape of the chamber.

The propeller and motor are mounted on a cylindrical pole, a distance of $3.34D$ away from the floor, and are centered with respect to each of the chamber's walls. They are oriented such that the thrust is directed downwards, toward the floor of the chamber. The propeller is surrounded by an array of 10 GRAS 40AE 1/2" pre-polarized free-field microphones. NI-9234 C-series sound and vibration modules are utilized to record signals from the microphone array.
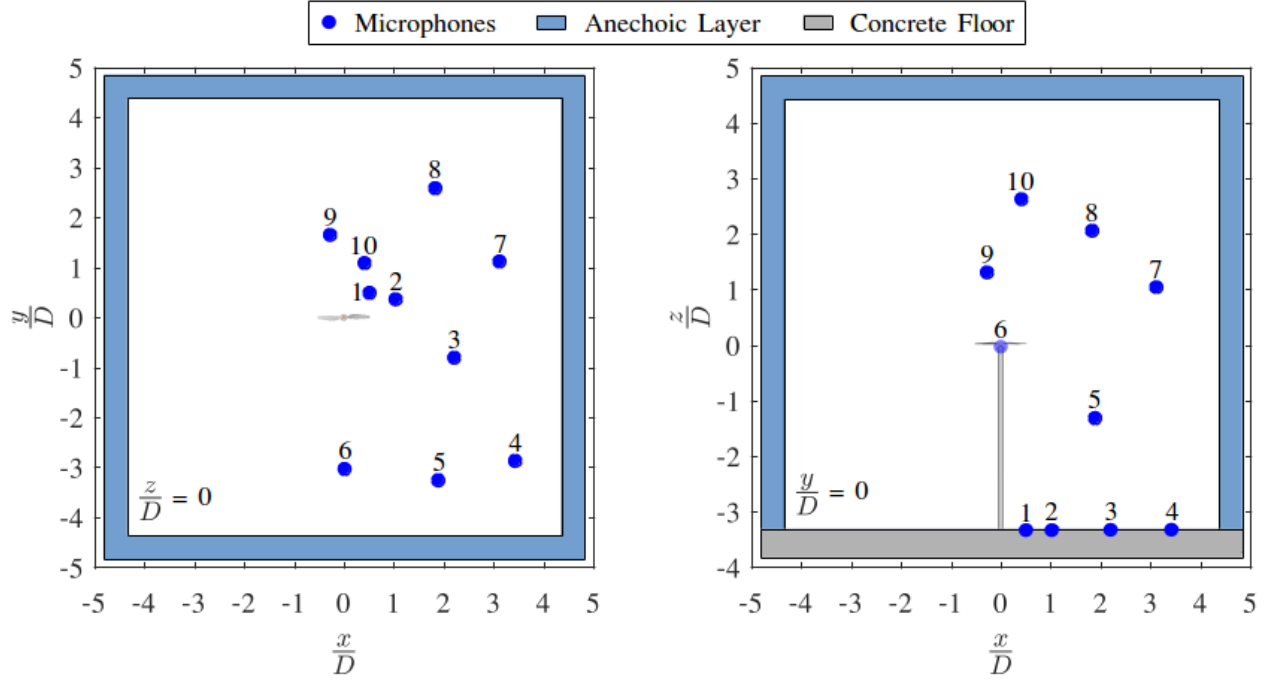
Fig. 1 Schematic of Amazon Prime Air's hemi-anechoic chamber, including the rotor test-stand and the microphone array configuration. The anechoic layer consists of sound-absorbing paneling and wedges.

The microphones in the array are positioned in such a way as to minimize noise from flow over them (wind-screens are also used) and any effects from standing waves in the chamber. They are individually calibrated using a B&K Type 4231 sound calibrator, with an accuracy of ±0.2 dB. The measurement errors are obtained from a comparison between a loudspeaker sound sample, as recorded at each microphone location, and its expected attenuation, which is inversely proportional to the stand-off distance from the source. We estimate that our measurement error at each microphone is approximately ±2 dB above a BPF harmonic of 2.2 and ±4 dB below that for any one 1/3-Octave band.

Lastly, propeller thrust and torque are measured utilizing an ATI Industrial Automation Gamma transducer, mounted between the motor and cylindrical pole. Same as for the signals from the microphone array, that from the load cell is recorded via an NI-9234 C-series sound and vibration module. Our calibration of the load cell with a known weight suggests that our measurements of thrust are accurate within 8.6×10^{-4} of the C_T, while those of torque are accurate within 3.6×10^{-5} of C_Q.

B. Measurement Protocol

The measurement protocol consists of steadily ramping up the angular speed of the rotor, until the target operating condition is achieved, and then holding the target operating condition until the aerodynamic loads on the rotor, as measured by the load cell, have reached a statistically steady state. Rotor angular speed is held within ±5 RPM for the duration of the test by a closed-loop motor controller. A five-second sound sample is then recorded at each microphone location, along with the thrust and torque at the load cell.

IV. Numerical Approach

A hybrid acoustic approach is used in this study to compute the noise radiated by a rotor under static condition. The unsteady flow field is computed using an LBM solver, whereas the acoustic far-field is computed using a surface integral approach based on the Ffowcs-Williams and Hawkings (FWH) acoustic analogy [2]. An acoustic porous medium (APM) model [3], which is based on the Darcy-law model for the bulk of the medium and a specific treatment of the solid interface between the fluid and the porous medium, has been used to simulate the presence of acoustic treatments in the anechoic test chamber. The APM layer absorbs the impinging acoustic waves but preserves the confinement effect of the

3

room responsible for the flow recirculation. A description of the methodology is provided in the following subsections.

A. Lattice-Boltzmann Method

The high-fidelity computational fluid dynamics (CFD) and computational aeroacoustics (CAA) software SIMULIA PowerFLOW 5.5b is used to compute the unsteady fluid flow and corresponding flow-induced noise mechanisms in the present study. The solver is based on LBM, which is intrinsically transient and compressible. The basic idea behind LBM is to statistically track the advection and collisions of fluid particles by an integer number of distribution functions aligned with predefined discrete directions. As in statistical physics, the flow variables such as density and velocity are determined by taking the appropriate moments, *i.e.*, summations over the set of discrete directions of the particle distribution function [4–6]. The relaxation time and other parameters of the equilibrium distribution function are computed by considering scales related to the turbulent motion of the resolved flow field. Such a procedure is usually referred to as very large-eddy simulation (VLES) and is based on the paradigm of a kinetic theory applied to a "gas of eddies". As discussed by Chen *et al.* [7], such an expansion of the kinetic theory leads to the fundamental observation that the Reynolds stresses, which are a consequence of the chaotic turbulent motion, have a non-linear structure and are better suited to represent turbulence in a state far from equilibrium, such as in the presence of distortion, shear, and rotation. In other words, although the relaxation time is computed using a two-equation transport model, the k-ε re-normalization group model in SIMULIA PowerFLOW 5.5b [7–10], it is not used to compute an equivalent eddy viscosity, like in Reynolds-averaged Navier-Stokes models, but is used to recalibrate the Boltzmann model to the characteristic time scales of turbulent flow motion. The fundamental turbulence modeling idea of viewing eddies as a gas system is much better justified at the Boltzmann level, involving an appropriate relaxation time, rather than the macroscopic level. SIMULIA PowerFLOW 5.5b has been previously validated for a variety of aerodynamic and aeroacoustic applications relevant to the present study, such as benchmark studies conducted for rotating devices [11–13], involving trailing-edge noise generation as a source of rotor/propeller broadband noise [14]. These studies also provide confidence in the prediction of propulsion-related quantities.

Following Zhang *et al.* [15], rotation can be incorporated by resolving the Lattice-Boltzmann equation in the rotating reference system and treating the non-inertial forces as external body forces. A local reference frame (LRF) volume region can be defined by creating a surface of revolution around the rotating solid part. The boundary of the volume of revolution is treated as a double-layer surface and the same boundary condition facetization algorithm is used to treat the two layers. Each surface layer communicates only with the inner (rotating) or outer (inertial) volume mesh. Conservation of normal and tangential momentum fluxes are imposed as a boundary condition on the two layers. During rotation, each layer collects mass and momentum and computes the distribution function based on the relative velocity. In the rotating volume, the local velocity is corrected by the acceleration terms.

B. Acoustic Porous Medium

For problems involving flow-induced noise, suitable CFD and/or CAA numerical methods are often non-linear and time-explicit. For a time-explicit solver, time-domain surface impedance boundary conditions could be used to model acoustic absorption due to porous materials. However, even when a time-domain surface impedance formulation can be derived, stability and robustness are challenging to achieve. Another possible approach and the one used in this project is to model absorbing materials as equivalent fluid regions such that sound waves travel through them. Analytical derivations show that the acoustic absorption is governed, or at least dominated, by the same physical mechanisms as flow resistivity. As a consequence, the same equations used to achieve the correct flow resistivity for a particular porous material also achieve the correct acoustic impedance. This approach is valid for any passive and homogeneous porous material [16]. As shown by Hersch and Walker [17], it is possible to analytically derive the expression for the impedance introduced by the presence of the porous medium. It is also possible to express the effects of a porous medium on the flow field due to an equivalent volume force acting on the fluid, which is related to the flow resistivity and the local flow velocity.

C. Ffowcs-Williams and Hawkings Method

LBM is inherently compressible and can be used to directly compute noise radiated from an unsteady flow past a rotating body. However, when the radiated noise has to be computed very far from the source region, as is usually the case for community noise applications, a hybrid approach must be used. In this approach, the computed near-field fluctuations are extrapolated to the far-field through an integral method. Two standard formulations are used in this

work, a time-domain formulation put forward by Farassat [18], based on the retarded-time solution of the FWH equation, and a forward-time, time-integration formulation [19]. The latter is a frequency-domain approach applied to the rotor surface [20, 21] which is assumed to be static. The frequency-domain formulation is used to highlight the broadband noise sources through a beam-forming (B-F) source identification, while its time-domain analog is used to predict both tonal and broadband noise components, which are then compared to measurements. The interest of using a frequency-domain formulation for the B-F analysis is related to its significantly lower computational cost, when compared to the time-domain formulation, when a large number of microphones is involved.

D. Computational Setup

The simulation for this study focuses on a fixed-pitch, two-bladed rotor. A single operating point is simulated with chamber temperature and pressure replicating the test conditions. The blade-tip Mach and chord-based Reynolds numbers are $M_c = 0.301$ and $Re_c = 2.6 \times 10^5$, respectively. The exact rotor and test rig geometry is considered in order to ensure accuracy of the predictions. The rotor is considered rigid and the nominal shape of the blades is used. The numerical model includes the test rig and the walls, celling and floor of the hemi-anechoic chamber, all located at the same position as in the experimental facilities.

To investigate the effect of flow confinement, two different models, one without and one with the walls and ceiling of the hemi-anechoic chamber, have been prepared. The first setup, referred to as "unconfined" herefrom, assumes negligible blockage: The computational volume spans $100D$ in all directions, with boundaries modeled as free-field using a pressure-outlet condition set to the chamber pressure, see Fig. 2 for a schematic. Two sponge layers are used to prevent acoustic waves from re-entering the computational domain. The layers are depicted in the schematic with green and red spheres, with the red layer having a higher absorption coefficient than the green one. The second setup, referred to as "confined" herefrom, adds a layer of APM around the rotor and test rig, and is shown in cyan in Fig. 2. The APM models the room walls and ceiling as solid for the flow and porous for the acoustics. The inner wall of the APM is positioned in agreement with the tip of the sound-absorbing wedges of Amazon Prime Air's hemi-anechoic chamber. For both setups, the sampling surface for the permeable FWH analysis is a sphere, with a diameter of $1.25D$ and centered on the rotor, shown in blue in Fig. 2.
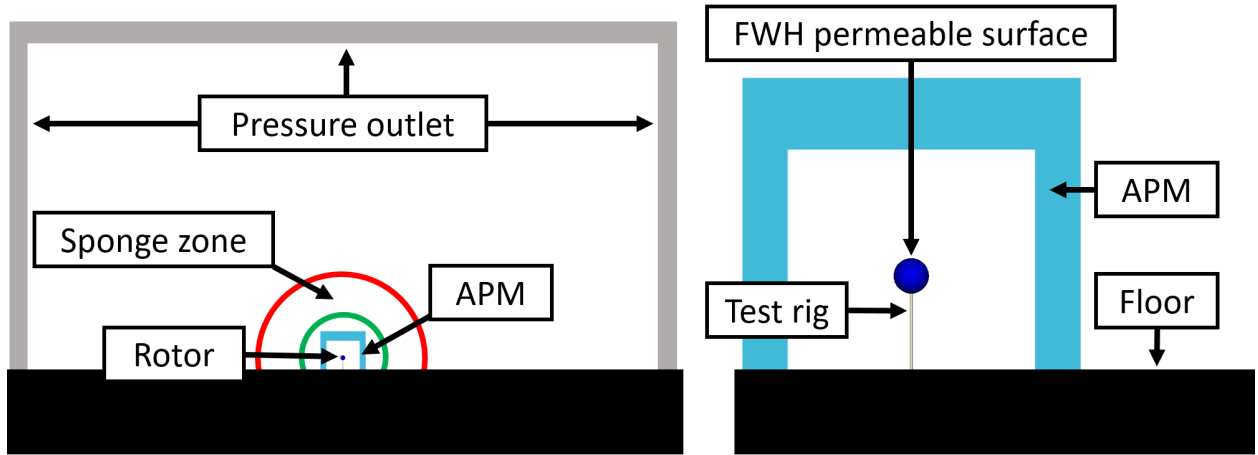

Fig. 2 Schematic of the simulation setup sliced along the rotor shaft's centerline. Full simulation volume (left) and close-up of the hemi-anechoic chamber (right).

The simulation volume is discretized with a Cartesian isotropic mesh using a cut-cell approach at the wall. The cell size on the blade is chosen so to obtain a minimum of 325 cells across the maximum chord of the blade, resulting in $y^+ \in (5, 70)$. The cell size between the rotor and the FWH permeable surface is chosen so to obtain a minimum of 15 points per wavelength, leading to a maximum resolvable frequency about 65 times larger than the BPF. The resulting mesh size is composed of 138 million volume elements. Each aeroacoustics simulation is run for an equivalent of 18 revolutions and the results are sampled for the last 10 revolutions. In order to speed up the statistical convergence of the aerodynamic field, the aeroacoustics simulation is initialized with the instantaneous velocity and pressure field resulting from a coarse simulation. The coarse simulation requires 18 and 990 rotor revolutions to achieve statistical convergence

5

for the unconfined and confined setups, respectively.

In order to ensure a fully turbulent boundary layer on the blade, a zig-zag trip, located at 20% of the local chord, is placed on the suction side of the blade, from the root up to 90% of the rotor's blade span. The local trip height is everywhere smaller than the local boundary layer thickness and is resolved with four cells across. As shown in previous studies [11–14], the presence of the trip triggers boundary layer transition without significantly altering the flow statistics far downstream, *i.e.*, 10 times the trip height an farther. The trip is expected to have a negligible influence on the rotor's thrust and a non-negligible influence on its torque.

The unconfined and confined simulations were completed in 47 and 74 hours, respectively, using 479 cores clocked at 2.9 GHz.

V. Comparisons between Simulations and Measurements

A. Aerodynamics

Table 1 reports the aerodynamic coefficients. The agreement in the coefficient of thrust between experiment and simulation is excellent, with simulation under-predicting the thrust by only 1.3%. Torque, on the other hand, is over-predicted by 8.6%. The latter can largely be attributed to the fact that boundary layer transition is not modeled in simulation, with a turbulent boundary layer assumed across the entire span of the blade. The zig-zag trip has a slight impact on C_T and a stronger impact on C_Q. It has been shown is previous studies [11–14] that although the trip geometry can affect the aerodynamics, it does not have a dominant effect on the aeroacoustics. Note that flow confinement has no impact on the averaged aerodynamic values, which is consistent with the observations of Stephenson *et al.* [1].

Table 1   Comparison of the coefficients of thrust, C_T, and torque, C_Q, between simulations and experiment.

	Trip	C_T	C_Q	Relative Error in C_T	Relative Error in C_Q
Unconfined Simulation	No	1.25×10^{-1}	8.99×10^{-3}	-1.3%	$+8.6\%$
Unconfined Simulation	Yes	1.23×10^{-1}	9.21×10^{-3}	-3.3%	$+11.3\%$
Confined Simulation	Yes	1.22×10^{-1}	9.25×10^{-3}	-3.4%	$+11.7\%$
Experiment	No	1.27×10^{-1}	8.28×10^{-3}	$-$	$-$

B. Aeroacoustics

Figure 3 shows an instantaneous view of the time derivative of pressure, which is proportional to the dilatation field, in the acoustic propagation region. The dominant tonal content and a rich broadband content can be observed. The traces of the tip vortices in the meridian plane clearly show the slipstream contraction effect. Finally, acoustic waves generated by the rotor and reflected by the floor can be seen traveling from the floor to the ceiling of the chamber.

The comparison of the predicted acoustic performance between experiment and simulation is presented by comparing the overall sound pressure level (OASPL) at the 10 microphone locations sketched in Fig. 1. The spectral content is compared by computing an approximation of the sound power Watt level (PWL) through integration of the acoustic intensity across circular strips between adjacent microphones. The same procedure is used to analyze the predicted and the measured noise spectra. Results for both the unconfined and confined simulations are reported. The A-weighted OASPL results are shown in Fig. 4. Interestingly, the effect of the flow confinement results in an almost constant offset of about 5 dBA, with the largest differences occurring at microphones close to the rotor axis. The discrepancy between measurements and simulation for the confined case is within 1.5 dBA for all microphones, which is smaller than the estimated experimental uncertainty of ±2 dBA. In what follows, we focus on the differences between the confined and unconfined simulations.

The narrow-band PWL spectral density is plotted in Fig. 5. The magnitude of the first BPF tone is perfectly captured by both simulations. This is to be expected, since this tone is related to the steady component of lift which has the same value for the two simulated cases, consistent with observations of Stephenson *et al.* [1].

The high-frequency part of the spectrum, starting from a BPF harmonic count of 30, is also insensitive to flow confinement. This part of the spectrum is blade self-noise due to the turbulent trailing-edge noise radiation phenomenon and/or blade-vortex interaction (BVI). Indeed, in hover conditions, the tip vortices remain quite close to the rotor plane
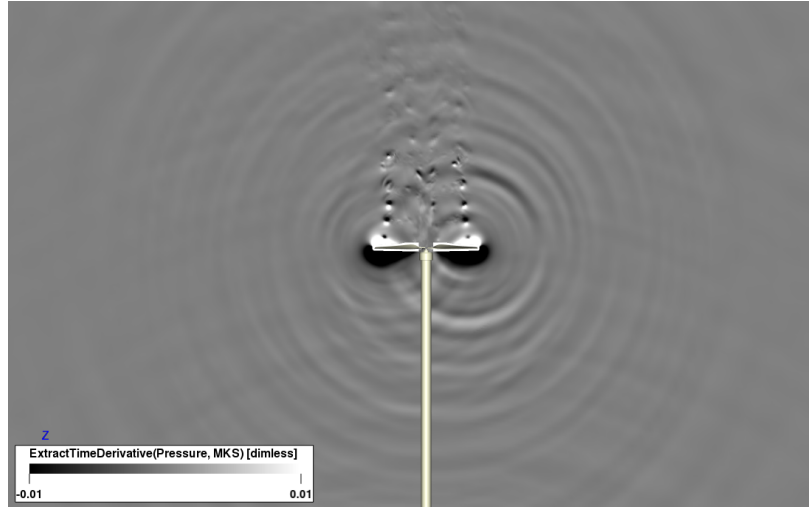
6

Fig. 3   Instantaneous snapshot of the time derivative of the pressure field sliced along the rotor shaft's centerline on a meridian plane.
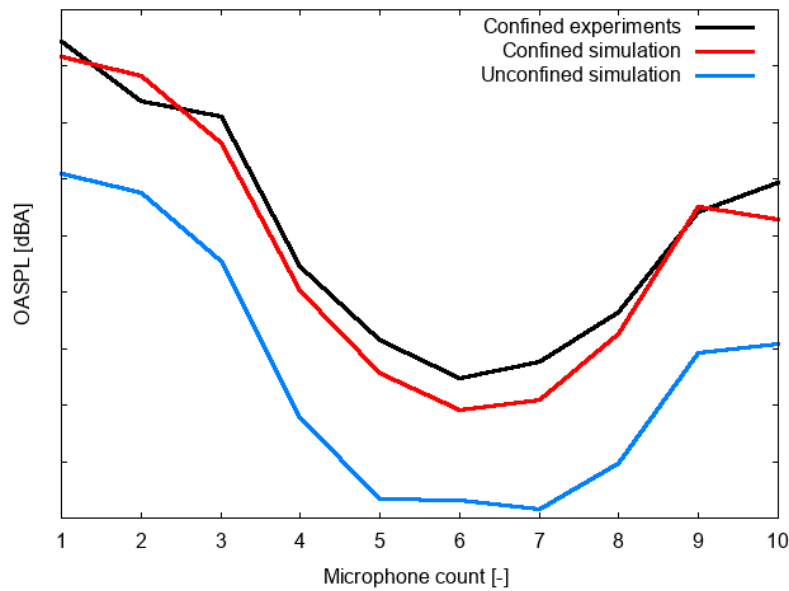

Fig. 4   OASPL for the unconfined simulation, confined simulation and experiment, computed at the 10 microphone locations around the rotor. The *y*-axis tics are 2 dBA apart.

and can induce a small unsteadiness on the blades that is similar in order of magnitude as the unsteadiness induced by the vortical structures generated in the boundary layer and convected past the trailing edge. Since BVI noise is very sensitive to the vortex/blade miss distance, a small increase of the axial velocity due to the recirculation in the room would be expected to significantly reduce BVI noise. However, a small noise increase is observed instead, which suggests that BVI plays a negligible role in high-frequency noise generation.

In the mid-frequency range, starting from a BPF harmonic count of 2 and ending at a count of 30, a very strong influence of flow confinement can be observed. Taking into account flow recirculation allows us to recover most of the tonal energy related to unsteady loading seen in the experiment. Hence, the main source of discrepancy between the two simulated cases should be the presence of additional unsteady blade loading in the confined case. A significant under-prediction of the first three BPF harmonics is also visible in the confined results. These spectral components could be related to large-scale eddies carrying enough energy to survive across several blade passages. Capturing these
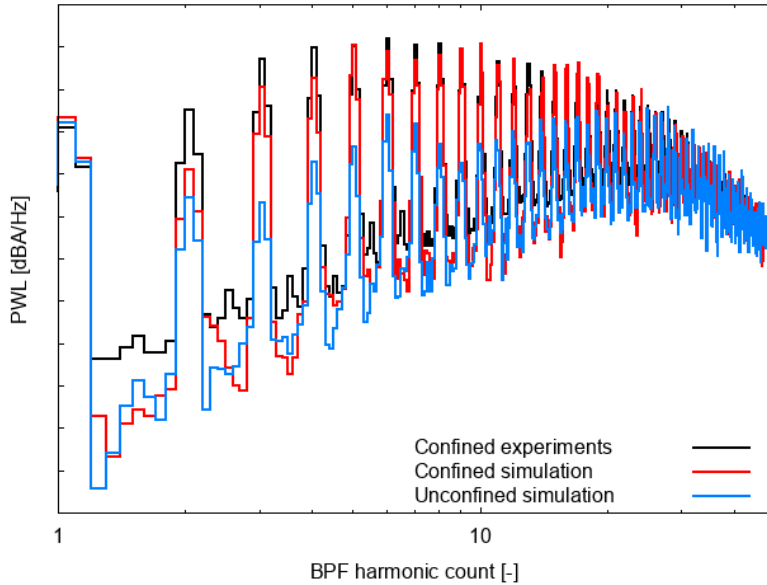
7

Fig. 5 PWL spectrum for the unconfined simulation, confined simulation and experiment, computed at the 10 microphone locations around the rotor. The *y*-axis tics are 5 dBA/Hz apart.

phenomena would require longer physical sampling times, long enough to converge low-frequency statistics and, in all likelihood, more realistic modeling of the test chamber, including details of the acoustic treatments applied to the walls. Some discrepancies between simulations and measurements can also be due to vibrations of the rig. A quantification of these effects will be the subject of future investigations.

Instantaneous flow field visualizations can support the hypothesis of additional unsteady loading in the confined case. Starting from Fig. 6, images of the tip vortex system are shown for the confined and the unconfined cases. As previously argued, the tip vortices remain very close to the rotor disk. They undergo a certain instability that induces the formation of small-scale vortices. Some of these vortices are located in the outer part of the slipstream and are washed down at a reduced speed compared to the mean stream. Therefore, they can induce unsteady loads in the tip region. The differences in the tip vortex between the two simulated cases are too small to explain the large difference in the radiated noise levels.
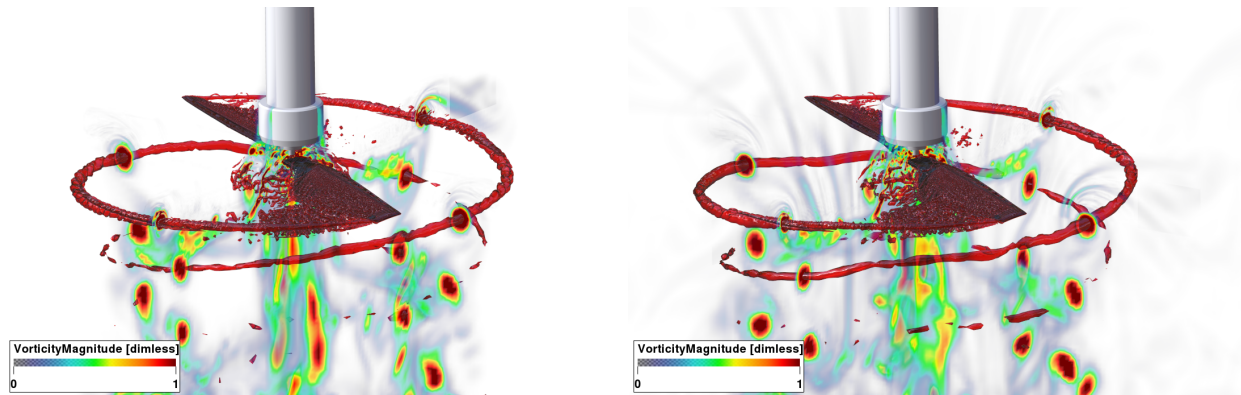

Fig. 6 Instantaneous λ_2 criterion iso-surfaces colored by vorticity magnitude and instantaneous snapshot of the vorticity magnitude field sliced along the rotor shaft centerline for the unconfined (left) and confined (right) simulations.

To explain the different noise levels, Fig. 7 shows contour levels of the vorticity field for the two cases. Besides the expected presence of vortical structures around the rotor for the confined case, it is interesting to observe that the

8

slipstream is also affected by the presence of these structures. Indeed, the annular region of the slipstream between the root and the tip vortices, which is a region of weak vorticity shed from blade locations characterized by small spanwise load variation, is significantly different in the two cases. Apparently, ingested vortical structures for the confined case are tilted, stretched and elongated in the axial direction. This phenomenon can lead to additional unsteady blade loading and generation of higher tonal noise levels.
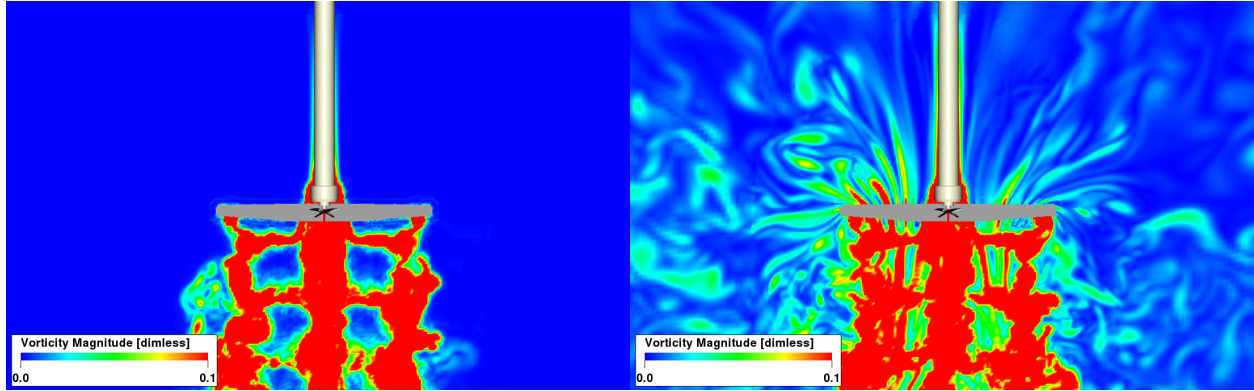
Fig. 7 Instantaneous snapshot of the vorticity magnitude field for the unconfined (left) and confined (right) simulations, sliced along the rotor shaft's centerline.

VI. Source Analysis and Physical Insight

Comparisons between measured and predicted noise spectra in the previous section pointed out the effects of flow confinement on the rotor noise. The main effect of blades interacting with turbulent structures convected by the recirculating flow is the significant enhancement of BPF harmonic peaks generated by unsteady loading. In this section the rotor noise source mechanisms are analyzed in more detail with the goal of highlighting the main differences between the rotor simulated in unconfined and confined conditions, and better discriminate between trailing-edge noise and BVI noise, if present. All plots shown in this section have tics on the y-axis every 5 dB, and show levels without A-weighting.

A. Analysis Process

Two analysis techniques are used. The first one consists of splitting one rotor blade in ten radial strips of equal spanwise extension, starting at 10% of the rotor's blade span, up to the tip, and performing a FWH integration of the different strips. The signals are computed along four semi-circles (meridians) of $21.2D$ in radius, equally spaced in the azimuthal direction. The duration of each signal corresponds to 10 rotor revolutions. Series of four signals at the same angular position with respect to the rotor axis and different azimuthal positions are appended and used to compute the source PWL, assuming an axisymmetric acoustic field [12]. A frequency bandwidth of BPF/10 (10 time-steps per blade passing period) and 13 Welch spectral averages (41.7% overlap) are used.

The second technique consists of performing a B-F CLEAN-SC deconvolution analysis in a rotor co-rotating reference system [22, 23], thus removing the effect of the periodic variation of the source-to-observer radiation vector, which is responsible for the Doppler projection of blade loading harmonics into acoustic BPF tones. A spiral antenna of outer diameter equal to about $30D$, coplanar with the rotor disk, and located at a distance of $3.3D$ from the rotor center is used. The microphones are distributed along 25 spires, with each spire consisting of 25 microphones for a total of 626, including the one located in the center of the array, as sketched in Fig. 8. The cross-spectral matrix is computed by using a frequency-domain FWH formulation applied to the rotor surface [20, 21]. The integrand is computed by using a bandwidth of BPF/2 and 16 Welch spectral averages (45.3% overlap). The B-F computation is performed in the BPF harmonic range 5 to 45. As already pointed out, the interest in using a frequency-domain FWH is its higher computational efficiency compared to the time-domain formulation when a large number of microphones is considered. For the sake of consistency, the agreement between the two FWH formulations is verified by comparing the spectra computed at the central microphone for both simulated cases, as shown in Fig. 9. Only negligible differences can be observed, which are due to the substantial differences between the two algorithms.

For both simulated cases, the quality of the B-F source identification is verified by comparing the spectra of the
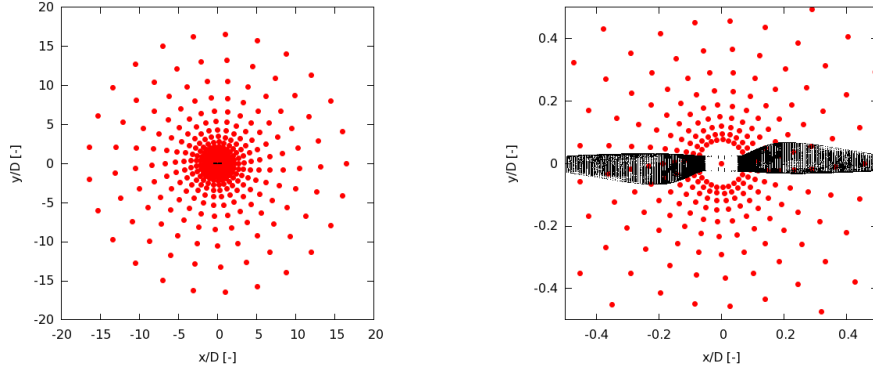
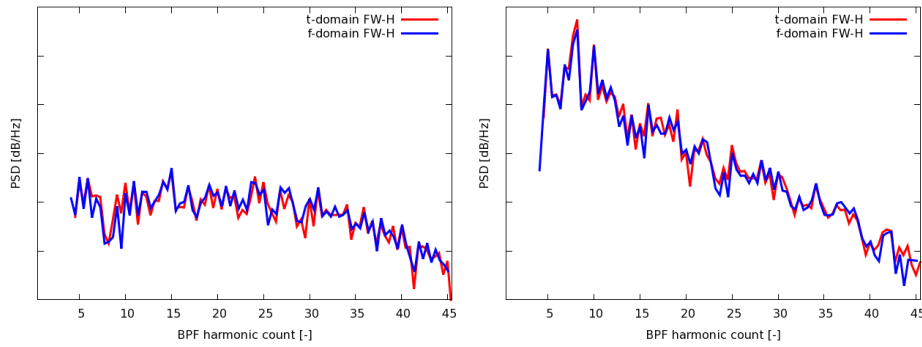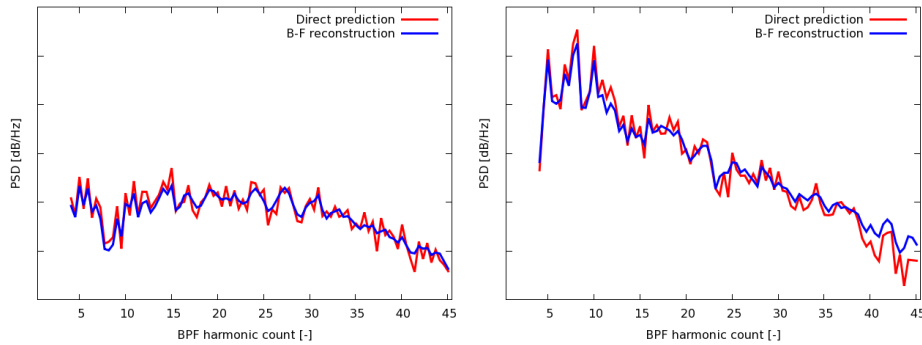**Fig. 8   Numerical B-F antenna, with grey dots denoting the rotor.**

Fig. 9   Noise spectrum at the array's central microphone for the unconfined (left) and confined (right) simulations. Comparison between the time- and frequency-domain FWH calculations.

input signals at the center of the array with noise spectra reconstructed via uncorrelated summation of the noise radiated from the B-F sources, as shown in Fig. 10. The agreement is very good in the explored frequency range, thus allowing us to rely on the identified sources. As discussed hereafter, the large difference between the two simulated cases is due to the higher radiation efficiency in proximity of the rotor axis in the presence of unsteady blade loading.

Fig. 10   Noise spectrum at the array's central microphone for the unconfined (left) and confined (right) simulations. Comparison between the direct FWH prediction and the B-F reconstruction.

B. Annular Strip Analysis Results

Before analyzing the differences between the two simulated cases in terms of spanwise source distribution, it is useful to highlight the difference in the overall noise radiation discussed in the previous section. Fig. 11 shows, for the

10

two cases, the PWL spectrum and the OASPL directivity. As expected, the interaction between the rotor blades and the turbulent flow structures convected by the recirculating flow in the confined simulation generates unsteady loads on the blades that, because of Doppler effects, are projected to higher BPF harmonics. The first two BPF tones are almost unaffected, whereas, starting from the third BPF harmonic, the tones for the confined results are about 5 to 10 dB higher than for the unconfined case. Such a different spectral behavior translates into about a 2 dB variation of OASPL at the maximum radiation angle of about 120 deg (ground side), where sky and ground refer to the real operating scenario and not the rig setup. Along the rotor axis, where the rotor-locked noise contribution tends to vanish, the confined case is up to 9 dB louder than the unconfined case, both towards the sky (0 deg) and the ground (180 deg).
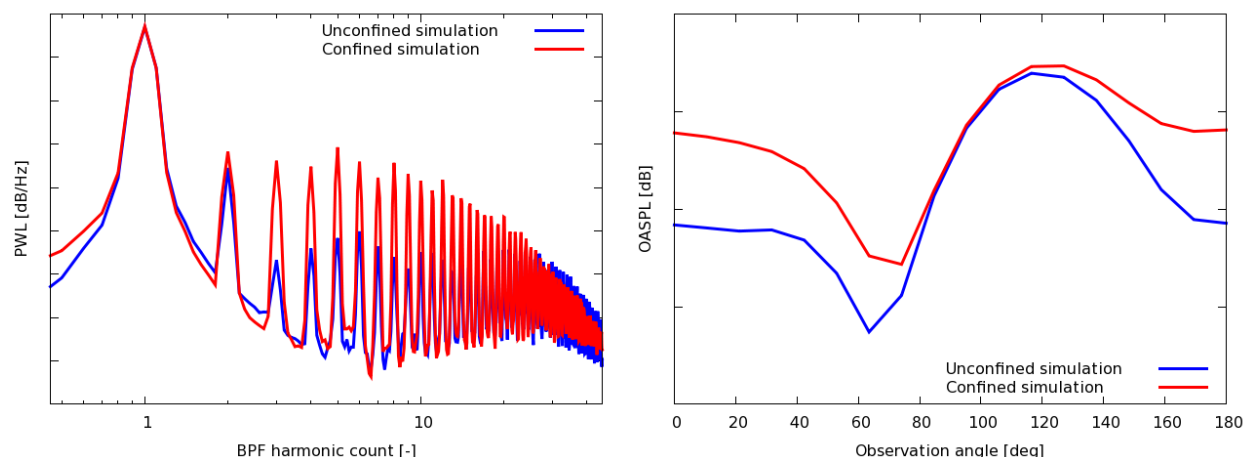

Fig. 11 PWL spectrum (left) and OASPL (right) for the unconfined and confined simulations. The zero-radiation angle corresponds to the suction side of the rotor's blades (sky).

The PWL spectra per blade strip are plotted in Fig. 12. Since one blade only is used for the FWH calculation, tones arise every half of a harmonic. The first interesting observation is that the effect of the unsteady loading due to the non-uniform rotor inflow is more prominent in the outer part of the rotor, with a clear emergence of tones in the last 20% of the span. The companion OASPL directivity plots are shown in Fig. 13. Interestingly, for both cases, the maximum noise radiation on the ground-side sector tends to move towards the axial direction. Moreover, the radiation pattern changes from a mono-lobe to a bi-lobe pattern moving from inboard to outboard strips. From a theoretical point of view, this behavior is related to the change of sign of the source-to-observer radial vector projected along the direction of the rotor lift.
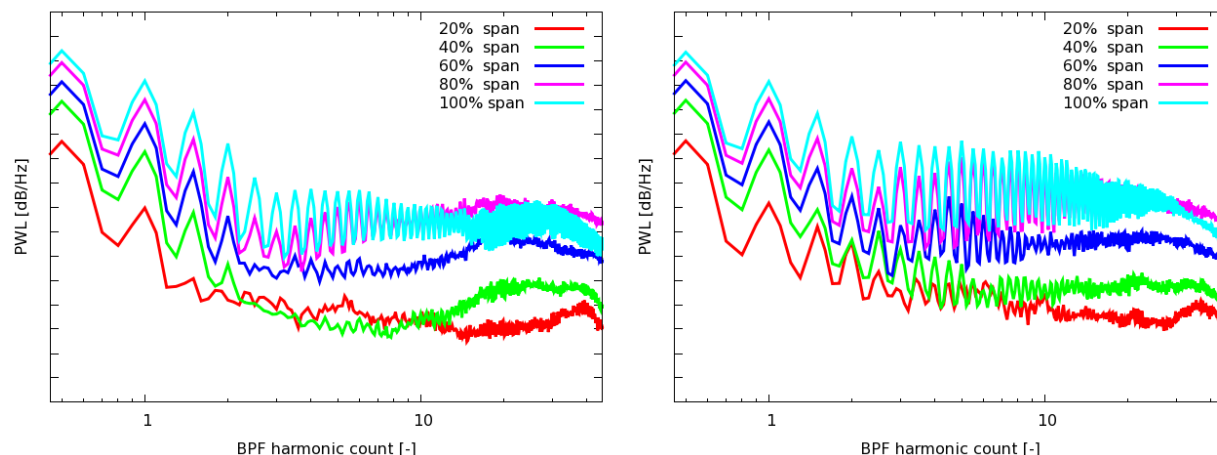

Fig. 12 PWL spectrum by radial strip for the unconfined (left) and confined (right) simulations.
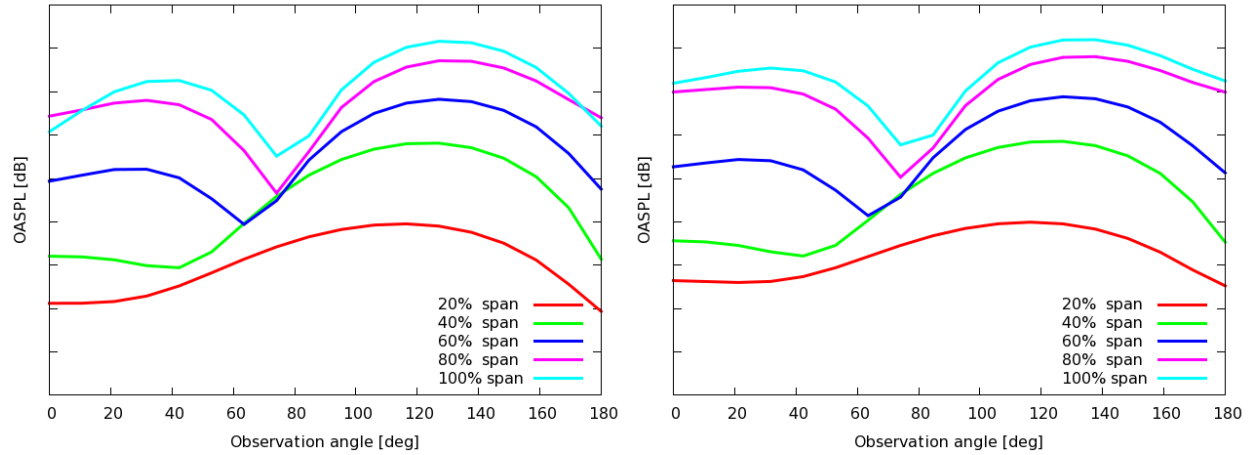
11

Fig. 13   OASPL directivity by radial strip for the unconfined (left) and confined (right) simulations.

A better quantification of the source power along the blade span is achieved by plotting the frequency-integrated PWL as a function of the strip radial location, as shown in Fig. 14. The two simulated cases have a very similar radial trend, corresponding to a cubic law (r^3), with slightly higher values for the confined case. Starting from about 50% of the explored span, the confined case exhibits a faster radially growing trend. The largest contribution to the blade interaction noise is therefore due to the unsteady flow in proximity of the blade tip. It is important to mention that the cubic radial dependence is a consequence of the variation of different Fourier components of the forces along the span and Doppler effects. An *a priori* prediction of this trend using theoretical arguments is not straightforward without knowing the spanwise variation of the unsteady blade loadings, which can be accurately predicted only via turbulence-resolved numerical flow simulations.
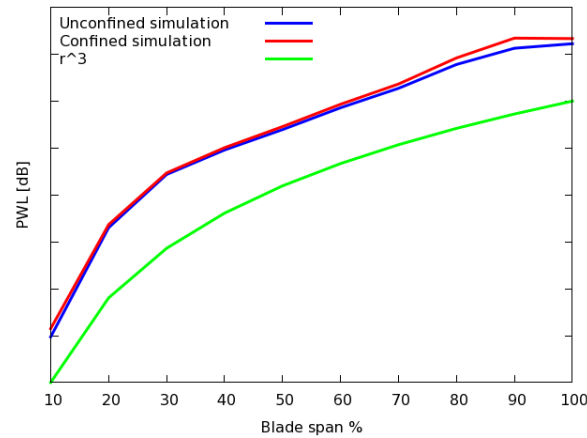

Fig. 14   Frequency-integrated PWL along the rotor's blade span for the unconfined and confined simulations.

Comparisons between the two cases for strips at 20%, 80% and 100% of the explored spanwise range, are shown in pairs of PWL and OASPL plots in Fig. 15. The OASPL directivity for the 80% strip confirms the highest contribution to the overall difference at the maximum radiation location. As already pointed out, the effect of the unsteady blade loading is to generate higher BPF tones that have a higher radiation efficiency along the rotor axis. Interestingly, the OASPL discrepancy at the maximum noise radiation angle seems to be generated in proximity of the 80% span.

C. Beam-forming Results
In this subsection, B-F maps are presented and discussed. Sources detected in narrow constant-frequency bands have been integrated in 1/3-Octave bands from band *N*, corresponding approximately to a BPF harmonic of 7, to band
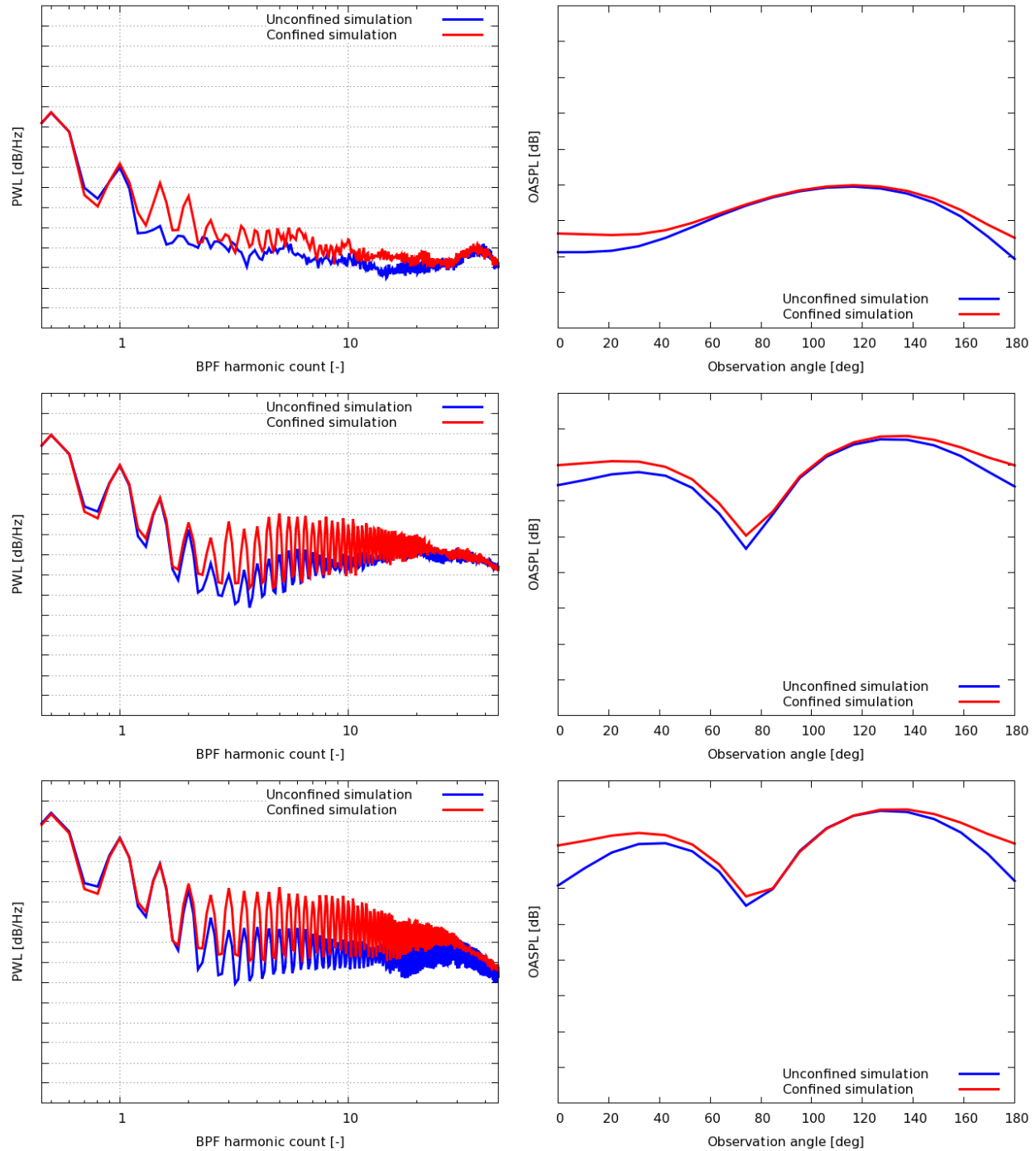
12

Fig. 15   PWL and OASPL from 20% (top), 80% (middle) and 100% (bottom) strips for the unconfined and confined simulations.

N+8, corresponding approximately to a BPF harmonic of 45. Contour levels of the source power level are plotted in Figs. 16, 17 and 18. In the low-frequency range (band N), the broadband noise sources for the unconfined case are more than 20 dB lower than for the confined case. Moreover, the confined results reveal that the noise sources are mostly aligned along the blade leading edge. A very similar trend can be observed for bands N+1 and N+2, besides a clustering of leading-edge sources in the 80% span region, thus confirming the findings of the blade strip analysis.
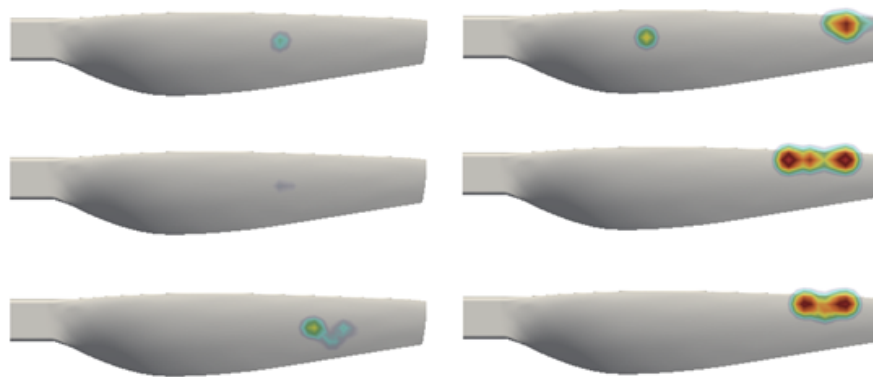
13

Fig. 16   B-F source maps for the unconfined (left) and confined (right) simulations, with 1/3-Octave bands N (top), $N+1$ (middle) and $N+2$ (bottom). Contour range: 20 dB.
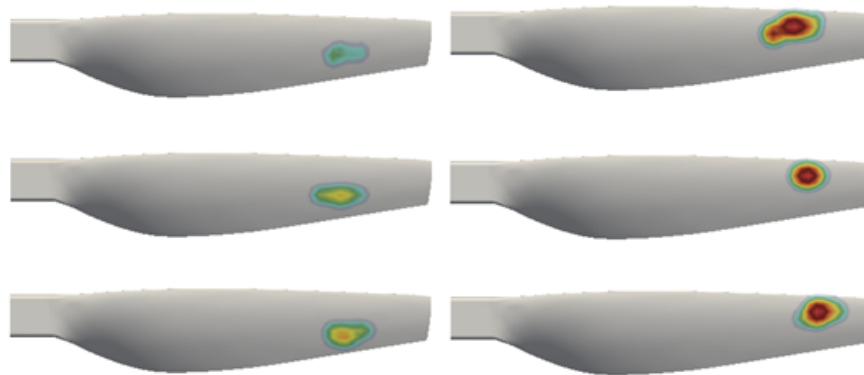

Fig. 17   B-F source maps for the unconfined (left) and confined (right) simulations, with 1/3-Octave bands $N+3$ (top), $N+4$ (middle) and $N+5$ (bottom). Contour range: 20 dB.

At higher frequencies, from band $N+3$ to band $N+5$, a dominance of the source strength for the confined case can be observed, but for these frequencies the sources for the unconfined case are clearly located along the trailing edge, whereas for the confined case, they are still located in proximity of the leading edge, slightly closer to the tip.

Finally, at the highest explored frequencies, for both cases, the noise sources are located in proximity of the trailing edge, and the levels between the two cases have similar order of magnitude. No differences can be observed in the tip region, thus excluding the possibility of a different BVI interaction mechanism between the two cases. Therefore, it can be argued that, for the confined case, the effect of the interaction between the blades and the convected flow perturbations is to slightly enhance the boundary layer turbulent fluctuations, but not to change the blade tip vortex dynamics, as already pointed out in the previous section.

The B-F maps constitute a reduced-order representation of the noise generation mechanisms. Similar insight can be achieved by inspection of the wall-pressure fluctuations on the pressure side of the blades. Here, the boundary-layer hydrodynamic fluctuations have a lower magnitude than on the suction side, thus allowing a clearer visualization of the acoustic pressure contribution scattered by the edges of the blade. Figs. 19, 20 and 21 show wall-pressure SPL in the same 1/3-Octave bands as for the B-F maps. The same *a posteriori* conclusions can be drawn: (i) leading-edge fluctuations dominate the lower frequency range of the confined case; (ii) trailing-edge contributions can be observed for both cases at all frequencies and tend to achieve similar levels for the two cases in the higher frequency range.
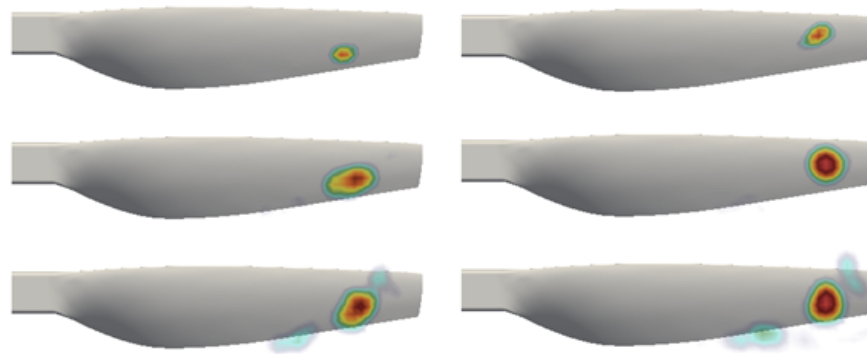
14

Fig. 18   B-F source maps for the unconfined (left) and confined (right) simulations, with 1/3-Octave bands N+6 (top), N+7 (middle) and N+8 (bottom). Contour range: 20 dB.

Interestingly, the tip region exhibits slightly higher levels for the confined case, a result that is not consistent with the B-F source localization. Additional analyses will be carried out in the future to better highlight the effect of the unsteady flow close to the tip on the radiated noise.
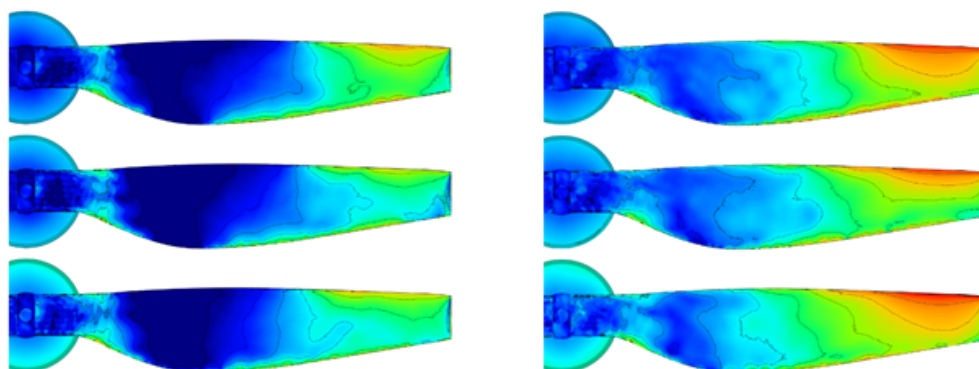

Fig. 19   Wall-pressure SPL on blade pressure side for the unconfined (left) and confined (right) simulations, with 1/3-Octave bands N (top), N+1 (middle) and N+2 (bottom). Contour range: 60 dB.

Fig. 20   Wall-pressure SPL on blade pressure side for the unconfined (left) and confined (right) simulations, with 1/3-Octave bands N+3 (top), N+4 (middle) and N+5 (bottom). Contour range: 60 dB.
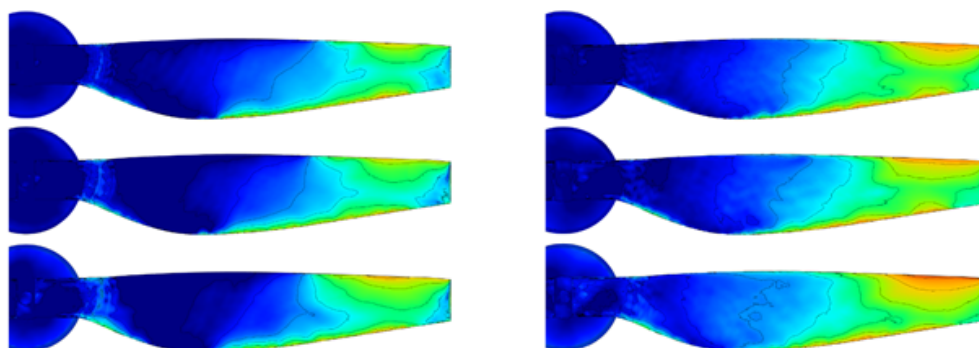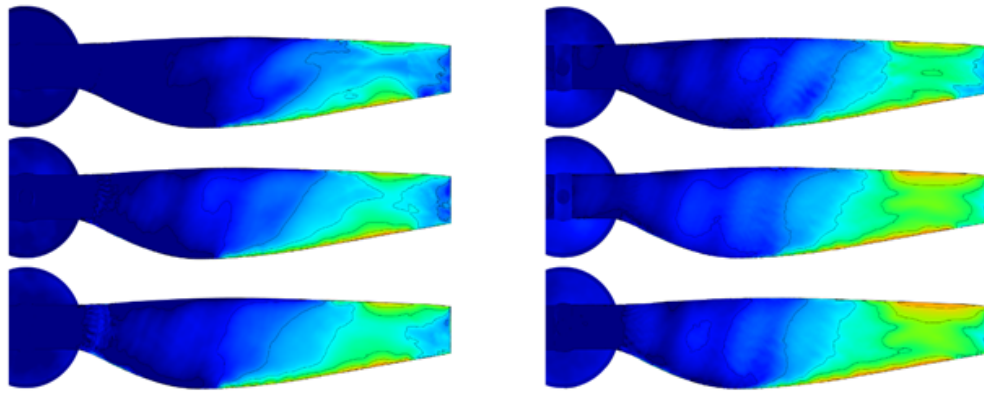
15

Fig. 21 Wall-pressure SPL on blade pressure side for the unconfined (left) and confined (right) simulations, with 1/3-Octave bands N+6 (top), N+7 (middle) and N+8 (bottom). Contour range: 60 dB.

VII. Conclusions

An experimental and numerical investigation was conducted to identify and characterize the effects of flow recirculation in a hemi-anechoic facility on the noise-generation mechanisms of a two-bladed, fixed-pitch drone rotor operating under static thrust conditions. Lattice-Boltzmann simulations were performed for both an idealized, semi-infinite free-field and a confined, hemi-anechoic domain that models the experimental setup. The latter was first validated against the experiment, with predictions of the rotor thrust and torque falling within −1.3% and +8.6% of the measurements, respectively, and the predicted and recorded OASPL agreeing to within 1.5 dBA of each other across all microphone locations. The relatively larger discrepancy in torque can at least partly be attributed to the absence of a laminar run across the rotor's blades in simulation. Next, results from the confined and unconfined simulations were compared to isolate the effects of flow recirculation. It was found that flow recirculation leads to a nearly 5 dBA increase in OASPL across most microphone locations, but has negligible impact on the thrust and torque of the rotor. Inspection of the narrow-band noise spectra revealed that the OASPL noise difference is related to the occurrence of higher BPF tones for the confined case due to the unsteady loading induced by the ingested turbulent structures recirculating in the test chamber. A deeper analysis of the sound-generation mechanisms through blade-strip and B-F source identification techniques revealed that the additional noise-generation mechanism is a leading-edge interaction, which is very effective in the low-to-middle frequency range and mostly localized around 80% of the rotor's blade span, and a slight enhancement of the trailing-edge noise mechanism in the high-frequency range. No effects due to BVI noise in the tip region were found.

Future investigations will focus on developing low-fidelity rotor noise models that account for some of the recirculation effects that have been identified in the present study. We expect these effects are important because drone rotors will routinely operate in non-ideal conditions, exposed to wind turbulence, ground effects, as well as other phenomena. In an optimization framework, a realistic low-fidelity noise model would be able to quickly reduce the design space to a handful of candidate rotors whose performance would be robust to off-design operating conditions. As importantly, the model's predictions could then be evaluated with the here-described Lattice-Boltzmann approach and, ultimately, validated in the hemi-anechoic facility.

References

[1] Stephenson, J. H., Weitsman, D., and Zawodny, N. S., "Effects of flow recirculation on unmanned aircraft system (UAS) acoustic measurements in closed anechoic chambers," *The Journal of the Acoustical Society of America*, Vol. 145, No. 3, 2019, pp. 1153–1155.

[2] Najafi-Yazdi, A., Brès, G. A., and Mongeau, L., "An acoustic analogy formulation for moving sources in uniformly moving media," *Proceedings of the Royal Society A: Mathematical, Physical and Engineering Sciences*, Vol. 467, No. 2125, 2010, pp. 144–165.

16

[3] Sun, C., Pérot, F., Zhang, R., Lew, P.-T., Mann, A., Gupta, V., Freed, D. M., Staroselsky, I., and Chen, H., "Lattice Boltzmann formulation for flows with acoustic porous media," *Comptes Rendus Mécanique*, Vol. 343, No. 10-11, 2015, pp. 533–544.

[4] Shan, X., Yuan, X.-F., and Chen, H., "Kinetic theory representation of hydrodynamics: A way beyond the Navier–Stokes equation," *Journal of Fluid Mechanics*, Vol. 550, 2006, pp. 413–441.

[5] Chen, H., Gopalakrishnan, P., and Zhang, R., "Recovery of Galilean invariance in thermal lattice Boltzmann models for arbitrary Prandtl number," *International Journal of Modern Physics C*, Vol. 25, No. 10, 2014, p. 1450046.

[6] Zhang, R., Shan, X., and Chen, H., "Efficient kinetic method for fluid simulation beyond the Navier-Stokes equation," *Physical Review E*, Vol. 74, No. 4, 2006, p. 046703.

[7] Chen, H., Orszag, S. A., Staroselsky, I., and Succi, S., "Expanded analogy between Boltzmann kinetic theory of fluids and turbulence," *Journal of Fluid Mechanics*, Vol. 519, 2004, pp. 301–314.

[8] Yakhot, V., Orszag, S., Thangam, S., Gatski, T., and Speziale, C., "Development of turbulence models for shear flows by a double expansion technique," *Physics of Fluids A: Fluid Dynamics*, Vol. 4, No. 7, 1992, pp. 1510–1520.

[9] Teixeira, C. M., "Incorporating turbulence models into the lattice-Boltzmann method," *International Journal of Modern Physics C*, Vol. 9, No. 08, 1998, pp. 1159–1175.

[10] Pervaiz, M. M., and Teixeira, C. M., "Two equation turbulence modeling with the lattice-Boltzmann method," *ASME-PUBLICATIONS-PVP*, Vol. 397, No. 1, 1999, pp. 15–24.

[11] Avallone, F., Casalino, D., and Ragni, D., "Impingement of a propeller-slipstream on a leading edge with a flow-permeable insert: A computational aeroacoustic study," *International Journal of Aeroacoustics*, Vol. 17, No. 6-8, 2018, pp. 687–711.

[12] Casalino, D., Hazir, A., and Mann, A., "Turbofan broadband noise prediction using the Lattice Boltzmann Method," *22nd AIAA/CEAS Aeroacoustics Conference*, 2016, p. 2945.

[13] Gonzalez-Martino, I., and Casalino, D., "Fan tonal and broadband noise simulations at transonic operating conditions using lattice-Boltzmann methods," *2018 AIAA/CEAS Aeroacoustics Conference*, 2018, p. 3919.

[14] Avallone, F., van der Velden, W., Ragni, D., and Casalino, D., "Noise reduction mechanisms of sawtooth and combed-sawtooth trailing-edge serrations," *Journal of Fluid Mechanics*, Vol. 848, 2018, pp. 560–591.

[15] Zhang, R., Sun, C., Li, Y., Satti, R., Shock, R., Hoch, J., and Chen, H., "Lattice Boltzmann approach for local reference frames," *Communications in Computational Physics*, Vol. 9, No. 5, 2011, pp. 1193–1205.

[16] Pérot, F., Freed, D., and Mann, A., "Acoustic absorption of porous materials using LBM," *19th AIAA/CEAS Aeroacoustics Conference, Berlin*, 2013.

[17] Hersch, A., and Walker, B., "Effect of grazing flow on the acoustic impedance of Helmholtz resonators consisting of single and clustered orifices," *The Journal of the Acoustical Society of America*, Vol. 72, No. 2, 1982, pp. 642–642.

[18] Farassat, F., and Succi, G. P., "The prediction of helicopter rotor discrete frequency noise," *38th American Helicopter Society Annual Forum, Anaheim, CA*, 1982.

[19] Casalino, D., "An advanced time approach for acoustic analogy predictions," *Journal of Sound and Vibration*, Vol. 261, No. 4, 2003, pp. 583–612.

[20] Lockard, D. P., "An efficient, two-dimensional implementation of the Ffowcs Williams and Hawkings equation," *Journal of Sound and Vibration*, Vol. 229, No. 4, 2000, pp. 897–911.

[21] Casalino, D., Santini, S., Genito, M., and Ferrara, V., "Rocket noise sources localization through a tailored beam-forming technique," *AIAA journal*, Vol. 50, No. 10, 2012, pp. 2146–2158.

[22] Sijtsma, P., "CLEAN based on spatial source coherence," *International journal of aeroacoustics*, Vol. 6, No. 4, 2007, pp. 357–374.

[23] Lockard, D. P., Humphreys, W. M., Khorrami, M. R., Fares, E., Casalino, D., and Ravetta, P. A., "Comparison of computational and experimental microphone array results for an 18% scale aircraft model," *International Journal of Aeroacoustics*, Vol. 16, No. 4-5, 2017, pp. 358–381.